A UAV-Aided Real-Time Channel Sounder for Highly Dynamic Nonstationary A2G Scenarios

Kai Mao, *Member, IEEE*, Qiuming Zhu, *Senior Member, IEEE*, Yanheng Qiu, Xin Liu, *Senior Member, IEEE*, Maozhong Song, Wei Fan, *Senior Member, IEEE*, André B. J. Kokkeler, *Member, IEEE*, and Yang Miao, *Member, IEEE*

***Abstract*— With the rapid development and broad applications of unmanned aerial vehicle (UAV)-based wireless stations in the sky, fundamental understanding and characterization of the realistic air-to-ground (A2G) communication link properties are crucial. In this article, a UAV-aided channel sounder with a real-time processing hardware system is developed for highly dynamic and nonstationary A2G channel measurements. In the hardware system, a global positioning system (GPS)-based triggering signal is designed, the equivalent antenna pattern affected by the UAV airframe is considered, and an appropriate sounding signal is selected, to improve the accuracy of measured channel impulse response (CIR). Moreover, real-time hardware processing algorithms for raw channel data, that is, CIR extraction, system response elimination (SRE), power loss recovery (PLR), and adaptive multipath component (MPC) recognition are developed and implemented on a single field-programmable gate array (FPGA) chip. In this way, the required storage size of channel data and the processing time for one slice of CIR is greatly decreased, which can meet the requirement of nonstationary A2G channel measurement with a high sampling rate and long-time measurement. A commercial channel emulator is used to reproduce controllable channels and verify the performance of the developed channel sounder. Finally, the developed channel sounder is applied to carry out A2G measurement campaigns at 3.5 GHz in a campus scenario. The channel characteristics, that is, path loss (PL), K-factor, and path angle are analyzed. The measured channel characteristics are consistent with existing measurements under a similar scenario. The estimated path angles are also validated by the theoretical results. Thus, the channel sounder can be used to capture the nonstationary A2G channel characteristics for the system design and algorithm optimization of A2G communications.**

***Index Terms*— Channel characterization, channel impulse response (CIR), channel sounder, nonstationary air-to-ground (A2G) channel, unmanned aerial vehicle (UAV) communications.**

Manuscript received 6 June 2023; revised 6 July 2023; accepted 13 July 2023. Date of publication 7 August 2023; date of current version 16 August 2023. This work was supported in part by the National Key Scientific Instrument and Equipment Development Project under Grant 61827801; in part by the National Natural Science Foundation of China under Grant 62271250; in part by the Natural Science Foundation of Jiangsu Province under Grant BK20211182; in part by the Key Technologies Research and Development Program of Jiangsu (Prospective and Key Technologies for Industry) under Grant BE2022067 and Grant BE2022067-3; in part by the Open Research Fund of National Mobile Communications Research Laboratory, Southeast University, under Grant 2022D04; in part by the China Scholarship Council; and in part by the Postgraduate Research and Practice Innovation Program of Jiangsu Province, under Grant KYCX22_0360. The Associate Editor coordinating the review process was Dr. Alessandra Galli. *(Corresponding author: Qiuming Zhu.)*

Kai Mao is with the Key Laboratory of Dynamic Cognitive System of Electromagnetic Spectrum Space, College of Electronic and Information Engineering, Nanjing University of Aeronautics and Astronautics, Nanjing 211106, China, and also with the Radio Systems Group, Faculty of Electrical Engineering Computer Science and Mathematics (EEMCS), University of Twente, 7522 NB Enschede, The Netherlands (e-mail: maokai@nuaa.edu.cn).

Qiuming Zhu, Yanheng Qiu, and Maozhong Song are with the Key Laboratory of Dynamic Cognitive System of Electromagnetic Spectrum Space, College of Electronic and Information Engineering, Nanjing University of Aeronautics and Astronautics, Nanjing 211106, China (e-mail: zhuqiuming@nuaa.edu.cn; qiuyanheng@nuaa.edu.cn; smz108@nuaa.edu.cn).

Xin Liu is with the School of Information and Communication Engineering, Dalian University of Technology, Dalian 116081, China (e-mail: liuxinstar1984@dlut.edu.cn).

Wei Fan is with the Antenna Propagation and Millimeter-Wave Systems Section, Department of Electronic Systems, Faculty of Engineering and Science, Aalborg University, 9220 Aalborg, Denmark (e-mail: wfa@es.aau.dk).

André B. J. Kokkeler and Yang Miao are with the Radio Systems Group, Faculty of Electrical Engineering Computer Science and Mathematics (EEMCS), University of Twente, Enschede, The Netherlands (e-mail: a.b.j.kokkeler@utwente.nl; y.miao@utwente.nl).

Digital Object Identifier 10.1109/TIM.2023.3301592

I. Introduction

UNMANNED aerial vehicles (UAVs) have been widely used in earthquake relief, forest fire detection, emergency rescue, and so on, due to their flexible deployment, low cost, and high mobility [1], [2], [3]. In the beyond fifth-generation (B5G) and sixth-generation (6G) communication networks, UAVs also have great potential as flying base stations or flying relays [4], [5], [6]. To ensure a reliable and effective UAV control or communication link, it is vital to deeply understand the radio propagation channel of UAV communications. Different from terrestrial communications, air-to-ground (A2G) communication has more obvious nonstationary and 3-D characteristics, that is, 3-D trajectory, 3-D scattering space, 3-D fuselage rotation, and height-dependence [7], [8], [9]. Here, "nonstationary" means the statistical properties of random channels change over time. In this article, it is also assumed the channel statistical properties keep unchanged within a small time period, namely stationary interval. Thus, traditional terrestrial channel models are not applicable anymore. With the development of UAV communications, the studies on A2G channel models have gained a lot of attention recently [10], [11]. Channel measurements are the foundation to observe, analyze, and model channel characteristics. However, the measurement campaigns for A2G channels are not sufficient so far, since there are no commercial A2G channel sounders as terrestrial channel sounders, and the existing ones have many restrictions in terms of flexibility and efficiency. Therefore, since the

instrumentation and measurement play an important role in the communication system [12], it is urgent to develop an efficient, reliable, and flexible A2G channel sounder to promote the standardization of UAV channel model and assist the design of UAV communication devices.

The typical channel sounding methods mainly include frequency-domain sounding (FDS) and time-domain sounding (TDS) [13], [14]. In the FDS-based method, the vector network analyzer (VNA) is utilized to measure the channel characteristics under indoor or static scenarios [15], [16], [17], [18]. Recently, Mbugua et al. [19], Schulpen et al. [20], and Xing and Rappaport [21] developed a fiber-based VNA sounder and extended the measurement range to hundreds of meters. However, applying it to dynamic A2G channel measurement is challenging, such as mounting the device with a fiber on the UAV. Note that Faul and Eibert [22] connected the UAV with VNA via an optical fiber for near-field antenna measurement, where the UAV moved slowly in a short range. However, it could bring security issues when the UAV moves rapidly over a long distance with the optical fiber.

The TDS-based method has been widely used in terrestrial mobile channel measurements [23], [24], [25], [26], [27], [28]. This method normally utilizes separate transceivers, which is also appropriate for A2G channel measurement. In this article, the transceiver means the aerial transmitter (TX) and ground receiver (RX) of the A2G channel sounder. With the development of UAV-aided communication, the A2G channel sounding and modeling have gained a lot of attention [11], [29], [30]. At the early stage, some large aircraft such as fighter aircraft [31], airship [32], [33], and fixed-wing [34], [35], [36], were used to carry heavy devices and perform the A2G channel measurement, but they were difficult to popularize due to high costs. Recently, the safety and stability of rotary-wing UAVs or drones have been greatly improved. Therefore, more and more A2G channel measurement campaigns were carried out by UAVs [37], [38], [39], [40], [41], [42], [43]. For example, some portable A2G channel sounders were designed and developed for the platforms as the quadcopter UAV [38], [39], hexacopter UAV [40], [41], and octocopter UAV [42], [43]. It can be found that most aforementioned channel measurement campaigns aim to obtain channel impulse responses (CIRs), which is also the main objective of our developed channel sounder.

However, there are still many challenges needed to be tackled for UAV channel sounders. First, the UAV airframe and the antenna position could significantly distort the antenna pattern and affect the extracted CIR. Most of the aforementioned A2G channel sounders adopted the original antenna pattern [32], [37], [40], [41], and only a few measurements involved the equivalent antenna pattern by considering the effect of UAV airframe [44], [45]. Second, the sampling time offset (STO) of transceivers due to the deviation of crystal oscillators could lead to uncertainty in the sliding correlation results [46]. To reduce this uncertainty, high-precision rubidium clocks were usually adopted in the terrestrial channel sounders [47], [48]. However, they usually are bigger and heavier, and the cumulative error of different rubidium clocks over a long-time channel measurement could not be ignored.

Last but not least, existing channel sounders stored the raw channel data (or baseband signals) in the disk and extracted channel characteristics offline [37], [38], [39], [40], [41]. For the dynamic A2G channel, each stationary channel state needs to be sampled within a small-time interval (i.e., smaller than the stationary interval). With the increase of bandwidth and antenna numbers, the sampled data rate could be up to tens of gigabytes (GBs) per second, which brings a great burden to the storage device. In other words, data storage and streaming are extremely important, especially when excessive data storage might be required for ultrawideband and MIMO channel sounding. Online processing is an alternative solution, which can greatly reduce the data transfer rate and total storage size as well as avoid tedious offline data processing. But traditional PC-based software online processing cannot meet the real-time requirement due to the rapid change of channel states. The comparison of several A2G channel sounders can be found in Table I. To address these issues, this article aims to mitigate the impact of: 1) UAV airframe to antenna pattern; 2) clock drift to sliding correlation; and 3) high sampling speed thus a large amount of data for storage capability, and to make the UAV A2G sounder performs robustly regardless of the three aspects. The contributions and novelties can be summarized as follows.

1) An efficient, accurate, and flexible UAV-aided channel sounder is developed for highly dynamic A2G scenarios. To achieve better measurement precision, the equivalent antenna pattern due to the UAV airframe is analyzed. It can eliminate about 10-dB variance of antenna gains in the path loss (PL) measurement. An L-type antenna array combined with an initial self-phase-calibration procedure is applied to guarantee accurate path angle estimation and flexible measurements. Moreover, an optimal channel-sounding signal is chosen by considering the complexity, spectrum flatness, and dynamic range.
2) To improve the accuracy and efficiency of the developed channel sounder, real-time hardware processing algorithms are developed and implemented in field-programmable gate array (FPGA) for the first time, that is, CIR extraction, system response elimination (SRE), power loss recovery (PLR), and adaptive multipath component (MPC) recognition. The maximum 6-dB loss of measured path power caused by the STO is well compensated. The measurement time for one slice of CIR decreases to 10.24 μs, which can capture the fast time-variant nonstationary channel characteristics under highly dynamic A2G scenarios. Meanwhile, by storing the path delays and amplitudes of valid MPCs instead of the whole continuous CIR, the required storage size decreases at least 100 times which enables long-time and large-space channel measurements.
3) The developed channel sounder is calibrated by using a commercial channel emulator which generates a reference and known channel with the path delay, amplitude, and phase to validate the correctness of

TABLE I
COMPARISON OF SEVERAL UAV CHANNEL SOUNDERS

Ref.	Frequency [GHz]	Bandwidth [MHz]	Sampling Interval of Each Snapshot	Antenna Pattern Affected by UAV Airframe	Consideration of STO Effect	Data Preprocessing	Storage
[37]	6.5	500	0.5 s	×	×	Software	Whole CIR
[38]	4.2	2200	—	×	×	Software	Whole CIR
	32	100 (Sweep)	0.5 s				
[39]	3.95	1700	100 ns (Not fully continuous)	×	—	Software	Whole CIR
[40]	2.5	15.36	—	×	✓	Software	Whole CIR
[41]	1.2 ∼ 6	120	34.13 μs	×	×	Software	Whole CIR
[45]	3.9	250	2 μs	✓	×	Software	Whole CIR
Our work	2.4/3.5	100	10.24 μs	✓	✓	Hardware Real-Time	Valid MPCs

measured channel characteristics. The measured channel parameters, that is, path delay, amplitude, and phase, agree well with the configuration settings, which verifies the reliability of processing algorithms and hardware implementation. Then, it is applied to carry out the channel measurement in a campus scenario, and the measured PL, K-factor, and path angle during takeoff, cruising, and landing of UAV are analyzed and compared with the existing measurements and theoretical results.

The rest of this article is organized as follows. Section II presents a UAV-aided A2G channel sounder with an equivalent antenna pattern and an optimal sounding signal. Section III develops and implements hardware processing algorithms, that is, CIR extraction, SRE, PLR, and MPC recognition on an FPGA chip, and the performance is analyzed and validated as well. In Section IV, the developed channel sounder is calibrated and applied in a real channel measurement in a campus scenario. Finally, conclusions are drawn in Section V.

II. UAV-AIDED A2G CHANNEL SOUNDER

A. Measurement System Setup

The whole system mainly consists of two parts, that is, the aerial TX and the ground RX, as shown in Fig. 1. The aerial TX includes a hexacopter equipped with a global positioning system (GPS) module, a TX software-defined radio (SDR) module with four radio-frequency (RF) channels, a high-power amplifier (HPA), and an omnidirectional dipole antenna. The sounding signal with different types and lengths are generated on an FPGA chip in the TX SDR module. The ground RX includes a reconfigurable L-type antenna array, four low-noise amplifiers (LNAs), an RX SDR module, a GPS module, and a high-rate disk array. The L-type antenna array has eight omnidirectional antennas, four in the azimuth plane, and four in the elevation planes. Moreover, a high-precision ruler is used to configure antenna positions for different measurement purposes. It should be mentioned that the proposed sounding system is capable of providing a continuous frequency band range while it is hard to find an antenna that works efficiently for the whole band. We choose a dedicated antenna for our

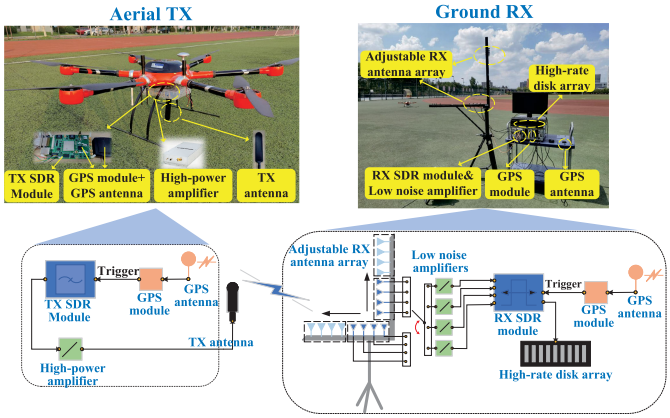

Fig. 1. Overview of the developed channel sounding system.

test experiments in Section IV-B due to its uniform antenna pattern and proper power gain. Note that the antenna can be easily replaced for other application scenarios at other bands. The processed data is stored in the high-rate disk array. In the ground receiving part, the programming environment of Labview FPGA developed by NI is utilized to implement the hardware algorithms. The Verilog HDL is also used to develop some component-level intellectual property (IP) cores for Labview FPGA. Note that an initial self-phase-calibration for RF channels will be performed for path angle estimation, that is, the azimuth angle of arrival (AAoA) and elevation angle of arrival (EAoA). The details of hardware components and features are listed in Table II. Note that the sampling rate of the developed channel sounder is 100 MHz, and the number of samples in each slice of the sounding signal is 1024, so the measurement period is 10.24 μs. The sampling period is adequate to distinguish the multiple paths is adequate to distinguish the multiple paths with a typical relative delay of hundreds of nanoseconds and capture the nonstationary UAV channels with millisecond-level stationery interval [49].

To guarantee the time synchronization of the transceiver, the one pulse per second (PPS) signals of the GPS module at the TX and RX are used to trigger the transmission of the sounding

TABLE II
SUMMARY OF HARDWARE COMPONENTS AND FEATURES

		Models	Features
Air TX	UAV	Customized	• Maximum payload = 8 kg • Flight endurance = 25 min
	GPS module	• UM220-IV N • GL-5 GPS antenna	• L1 frequency = 1575.42 MHz • Accuracy of 1PPS (RMS) = 20 ns
	TX SDR module	Customized	• Frequency range = 70 MHz-6 GHz • Bandwidth = 100 MHz
	High-power amplifier	Mini-Circuits ZHL-2W-63-S+	• Frequency range = 600-6000 MHz • Gain = 42 dB
	TX antenna	PulseLarsen Antennas SPDA24617/3900	• Frequency range = 617-960/1400-2700 /3200-3900 MHz • Omni azimuth pattern/110 degrees elevation pattern • Gain = 1/2.5/3 dBi
Ground RX	RX antenna array	L-type Antenna Array TYMA010	• 8 antennas in the azimuth/elevation planes • Frequency range = 2.3-2.5/3.4-3.6 GHz • Omni azimuth pattern/120 degrees elevation pattern • Gain = 0 dBi
	Low noise amplifier	YJLNA1030	• Frequency range = 1000-4000 MHz • Gain = 38 dB
	RX SDR module	• NI PXIe-1085 chassis • PXIe-8135 controller • PXIe-7976 module • PXIe-5791 RF adapter	• FPGA = Xilinx K7 410T • Frequency range = 200-4400 MHz • Bandwidth = 100 MHz
	High-rate disk array	NI HDD-8266	• Disk capacity = 24 TB • Data transferring rate = 3.6 GB/s
	GPS module	• NI PXIe-6683 • GL-5 GPS antenna	• L1 frequency = 1575.42 MHz • Accuracy of 1PPS (RMS) = 15 ns

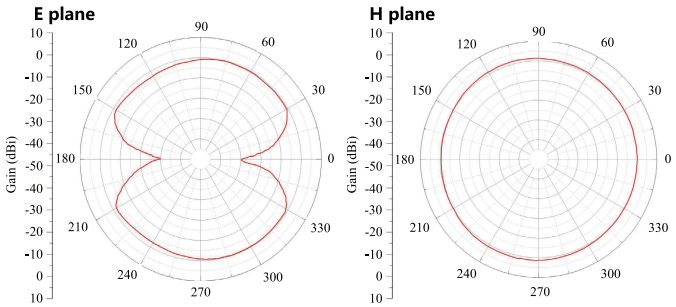

Fig. 2. Antenna patterns of the ground RX.

signal and processing of the receiving signal, respectively. In this case, the absolute path delay (or the length of the line-of-sight path) can be determined. In addition, the PPS signal deviation of different GPS modules may cause several meters error, which is acceptable for a typical hundreds-meter UAV communication distance.

B. Antenna Placement

Each antenna element of ground RX has an approximately omni azimuth pattern and a 120° elevation pattern at half-power beamwidth (HPBW) as shown in Fig. 2. Thus, the sounder system can receive most of the arrival signals from different AoAs but not directly on top of it. Since the tripod and antenna holder are simple, this article ignores their effects on the antenna pattern. However, the antenna pattern at the aerial TX may significantly change due to the shadowing and reflections of the UAV airframe. Thus, the installation position should be carefully considered to reduce this effect [29]. In this article, the omnidirectional sounding antenna at the UAV has an approximately omni azimuth pattern and a 110° elevation pattern at HPBW. Mounting the antenna on the bottom of the UAV fuselage and a rotary wing, the equivalent antenna pattern on the UAV is compared in Fig. 3(a) and (b), respectively. It can be found that the pattern variance on the E-plane is larger than that on the H-plane. Mounting the antenna on the bottom of the UAV fuselage has a better performance for channel measurement. However, the variation of the antenna pattern on the E-plane still needs to be eliminated in the data processing.

The above original antenna patterns are obtained from the measured results of manufacturers. The equivalent antenna patterns affected by the UAV airframe are obtained from the simulation results of CST Studio Suite.

C. Sounding Signal

Common channel sounding schemes include continuous waveform (CW)-based schemes, narrow-pulse-based schemes, correlation-based schemes, and so on. These sounding schemes have different advantages and disadvantages in terms of implementation complexity and measurement ability. The CW-based sounding scheme is normally used to measure large-scale fading and shadowing (i.e., narrowband power measurement). It is a single-tone power-only measurement, and therefore it is not possible to obtain CIRs. The narrow-pulse-based sounding scheme is suitable for capturing the information of MPCs without complex data processing, but it has poor antinoise performance and low transmission efficiency. In our A2G sounder, the correlation-based sounding scheme is employed for capturing MPCs and for long-distance measurements, where pseudo-noise (PN) and Zadoff-Chu (ZC) sequences are two commonly used sounding signals.

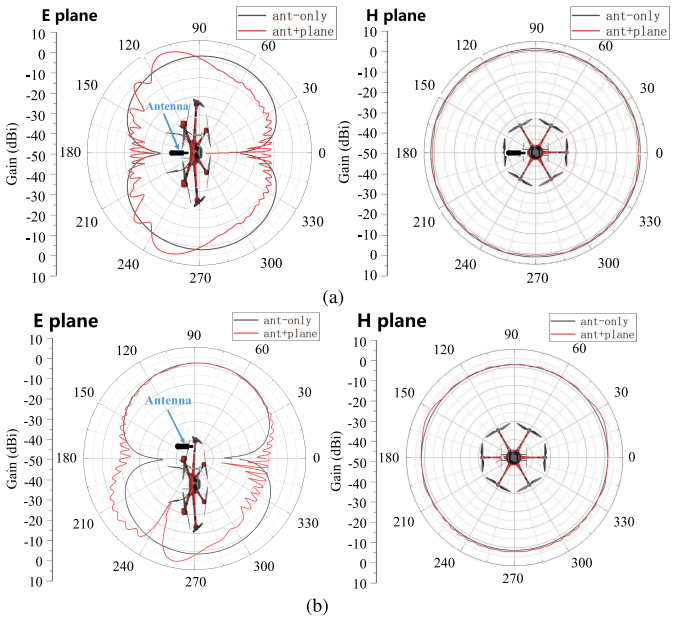

Fig. 3. Equivalent antenna patterns with the antenna mounted on the bottom of (a) UAV fuselage and (b) rotary wing.

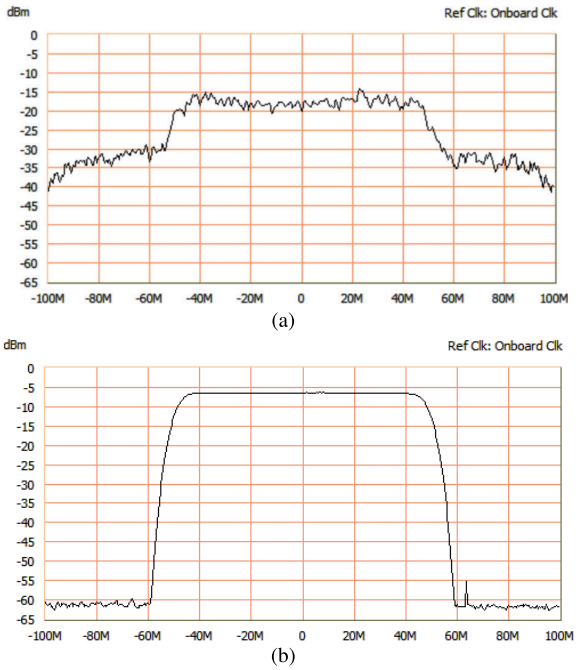

Fig. 4. Comparison of spectral flatness for (a) PN and (b) ZC sequence.

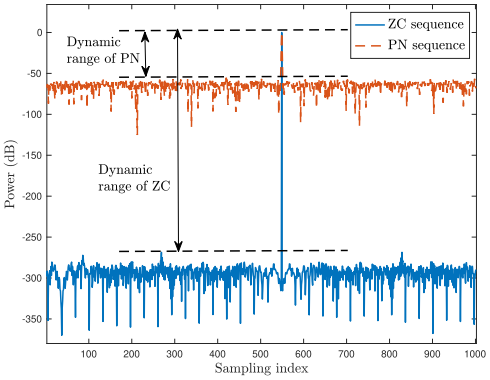

Fig. 5. Comparison of the theoretical dynamic range.

We choose the ZC sequence instead of the PN sequence, because of the following considerations.

1) *Complexity:* As a digital binary sequence, the PN sequence needs a shaping filter to make it suitable for the subsequent modulation and transmitting, especially in the preliminary simulation procedure. However, the ZC sequence is suitable to be modulated and transmitted directly. In addition, different generation functions are needed for the PN sequences with different types and lengths, while the ZC sequence has a uniform generation function as in [50]

$$s[n] = \begin{cases} \exp\left(-\dfrac{j\pi\mu n^2}{N_{\mathrm{ZC}}}\right), & N_{\mathrm{ZC}} \text{ is even number} \\ \exp\left(-\dfrac{j\pi\mu n(n+1)}{N_{\mathrm{ZC}}}\right), & N_{\mathrm{ZC}} \text{ is odd number} \end{cases} \tag{1}$$

where $n = 0, 1, \ldots, N_{\mathrm{ZC}} - 1$, and N_{ZC} and μ are used to control the length and type, respectively. Note that μ is less than N_{ZC} and relatively prime to N_{ZC}. The maximum-length sequence, also known as the m-sequence, is employed as a case of the PN sequence for comparison purposes. When generating m-sequences with different sequence lengths, different primitive polynomials are needed that can be found in the lookup table with primitive polynomials for m-sequences. In this article, we use the primitive polynomial "$x^{10} + x^3 + 1$."

2) *Spectral Flatness:* To obtain the accurate frequency transfer function, the sounding signal should have good spectral flatness over the whole channel bandwidth. Taking the ZC and PN sequence with a length of 1024 as an example, the sequences are generated on FPGA with a sampling rate of 100 MHz and the corresponding spectrums can be observed by a spectrum analyzer (NI VST-5840). Note that the bit-width of the DAC in the FPGA module is 16 bits, and the bandwidth of the generated sounding signals is 100 MHz. The comparison of spectral flatness within bandwidth 100 MHz is shown in Fig. 4, which indicates that the ZC sequence has better spectral flatness.

3) *Dynamic Range:* Dynamic range of the channel sounder is an important factor for the detection ability of weak paths. It can be defined as the ratio of the sliding correlation peak (SCP) to the maximum interference [51] as shown in Fig. 5. Without considering the noise, the dynamic ranges of PN and ZC sequence with the length of 1024 are shown in Fig. 5. It can be found that the theoretical dynamic range of the ZC sequence is much larger than that of the PN sequence.

III. Real-Time Data Processing Based on FPGA

A. Real-Time Parallel CIR Extraction and SRE

In the developed A2G channel sounder, the sounding signal at the TX is carefully designed such that its autocorrelation function can well approximate a delta function, and the CIR

can be extracted at the RX as [41]

$$\hat{h}(t,\tau) = y(t) \otimes s(t) = h(t,\tau) * s(t) \otimes s(t) \quad (2)$$

where $s(t)$ is the sounding signal, $y(t)$ is the received signal, $h(t,\tau)$ is the real channel under measurement, $*$ is the convolution operator, and $\otimes$ is the sliding correlation operator. Once the autocorrelation of the transmitting signal approaches a delta function, we can retrieve the CIR.

The software-based sliding correlation operation (SCO) was commonly used to extract the channel characteristics [35], [52]. However, it consumes a large storage source and needs a high data transfer rate to store raw data in real time. To overcome this shortcoming, this article develops a real-time parallel SCO hardware algorithm on the FPGA.

Defining the transmitted ZC sequence as $s[n]$ and the received baseband signal as $y[n]$ in the discrete time domain, the SCO of (2) can be rewritten by a circular convolution operation as

$$h_{\mathrm{SCO}}[n] = y[n] * \hat{s}^*[n] \quad (3)$$

where $\hat{s}[n]$ is the reverse sequence of $s[n]$, $(\cdot)^*$ is the conjugate operator, and $*$ is the convolution operator. The channel transfer function (CTF) in the frequency domain can be expressed as

$$H_{\mathrm{SCO}}[k] = Y[k] \cdot \hat{S}^*[k] \quad (4)$$

where $Y[k]$ and $\hat{S}^*[k]$ are the fast Fourier transform (FFT) of $y[n]$ and $\hat{s}^*[n]$, respectively. Thus, the CIR can be obtained by performing the inverse FFT (IFFT) of CTF. As shown in Fig. 6, we develop a parallel framework of (4) to extract the CIR on an FPGA chip in real time. The circular read-only memory (ROM) is used to store the local ZC sequence $s[n]$, and $\hat{s}[n]$ is obtained by reading the ROM in reverse. Then the FFT and multiplication operation are performed to implement (4). Combined with the real-time MPC extraction in Section III-C, our channel sounder system can save lots of storage resources and greatly ease the burden of data transfer.

Note that the original extracted CIR $h_{\mathrm{SCO}}[n]$ involves not only the measured channel response, but also the hardware system response including filters, HPA, LNA, and so on. According to the preliminary comparison tests, we found that the filters and other devices in the SDR module in the developed channel sounder have limited effect on the measured CIR, while the power amplifiers would bring in some unexpected peaks and increase the noise level. Therefore, it is crucial to eliminate these hardware system responses. In this article, the hardware system response is obtained by a back-to-back measurement and removed in the field measurement. In the back-to-back measurement, we connect the transceivers of the channel sounder directly via the same RF cable used in the field measurement. Then, the same SCO procedure in (4) is performed at the RX to obtain the CTF of the hardware system. The CIR after SRE can be expressed as

$$h_{\mathrm{SRE}}[n] = \mathrm{IFFT}(H_{\mathrm{SCO}}[k]/G[k]) \quad (5)$$

where $\mathrm{IFFT}(\cdot)$ is the inverse Fourier transform and $G[k]$ denotes the CTF of hardware system.

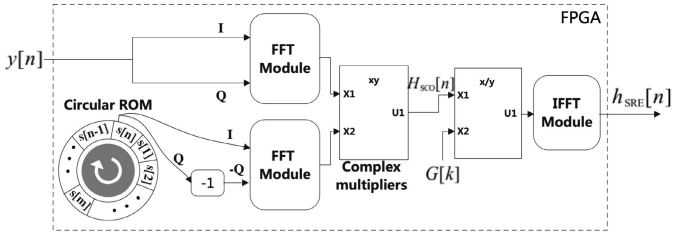

Fig. 6. Real-time parallel structure of SCO and SRE.

B. Real-Time PLR

In the back-to-back measurement, as the transceivers are connected directly, one SCP can be obtained by performing the SCO procedure in Section III-A. This SCP should be constant, but we found out that the measured SCP is time-variant and periodic in the back-to-back measurement as shown in Fig. 7(a). The main reason for that is caused by the STO of transceivers [46]. Note that we do not aim to measure the exact value of the STO. The purpose of this section is to study how the STO affects the measured CIR and find a solution to compensate for this effect. In this way, we can avoid measuring and compensating random STOs. Therefore, this section follows the story line of measurement observation, theoretical derivation, proposed solution, and validation and comparison.

Taking a 40-MHz crystal oscillator as an example, if the frequency deviation is 15 parts per million (PPM), the maximum STO between the transceiver can reach up to 1200 Hz. Set the sampling rates of TX and RX as f_{TX} and f_{RX}, respectively, and the STO as $\Delta f = f_{\mathrm{RX}} - f_{\mathrm{TX}}$. It can be derived that the SCP has a maximum 6-dB power loss caused by STO. The derivations in detail can be found in the Appendix. Moreover, the period of SCP power loss can be calculated as

$$D_{\mathrm{STO}} = \frac{1/f_{\mathrm{TX}}}{|1/f_{\mathrm{RX}} - 1/f_{\mathrm{TX}}|} \cdot (1/f_{\mathrm{RX}}) = \frac{1}{|f_{\mathrm{RX}} - f_{\mathrm{TX}}|} = \frac{1}{|\Delta f|} \quad (6)$$

which is only related to Δf. The cumulative power loss under different STOs, that is, 0, 200, 500, and 1000 Hz are presented in Fig. 7(b). It can be found that the maximum cumulative power loss reaches 6 dB, which cannot be ignored, and the power loss varies faster when the STO is increasing.

To compensate for the power loss caused by STO, Burmeister et al. [46] proposed a recovery method by using sinc-interpolation. However, this method severely reduced the dynamic range of measured CIR. Moreover, the CIRs needed to be oversampled. In [46], an oversampling factor of 20 was utilized to achieve a good recovery performance. Taking the sampling rate of 100 Ms/s as an example, a 1-Gs/s sampling rate is needed for even ten-time oversampling, which is not practical for the hardware implementation. To address this issue, we propose a PLR method as

$$h_{\mathrm{PLR}}[m] = \sum_{n=m-2\varepsilon}^{m} h_{\mathrm{SRE}}[n] \cdot \mathrm{sinc}\left(\frac{m-n}{I}\right) \quad (7)$$

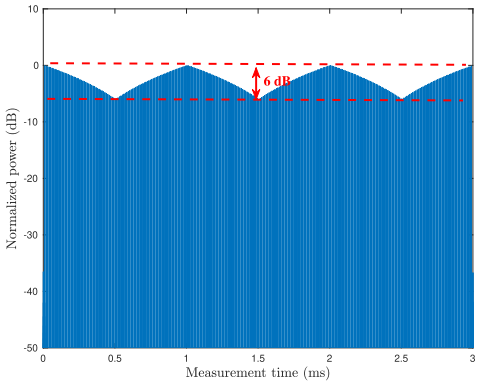

(a)

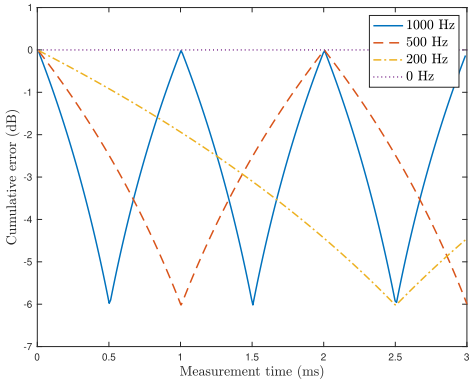

(b)

Fig. 7. (a) SCPs and (b) cumulative power loss of SCPs under different STOs.

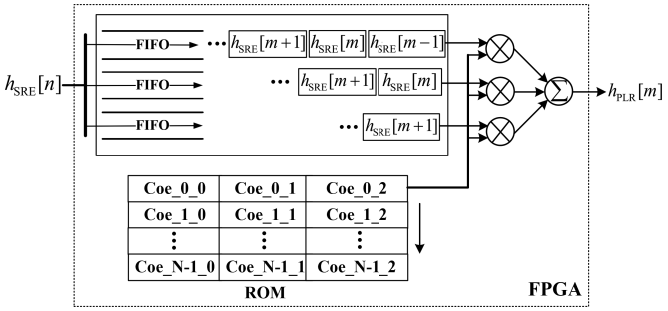

Fig. 8. Real-time polyphase structure of PLR.

where $m = 0, 1, \ldots, N_{ZC} - 1$, N_{ZC} is the length of $h_{SRE}[n]$, I is the oversampling ratio of sinc filter, and ε is the width of recovery window. It can be found that $h_{SRE}[-2]$ and $h_{SRE}[-1]$ are invalid values. This is because there is an initial pipeline latency of $2\varepsilon+1$ clock cycles before the first valid output. But this situation only occurs at the beginning of hardware system booting. For example, the second slice of CIR will start from $h_{SRE}[N]$, thus $h_{SRE}[-2]$ and $h_{SRE}[-1]$ turn into $h_{SRE}[N-2]$ and $h_{SRE}[N-1]$. To make the tradeoff of recovering performance and pipeline latency, ε is recommended to be set between 1 and 4. In (7), we only oversample the coefficients of the sinc filter instead of the whole CIR, which is easier for the hardware implementation. Moreover, a polyphase hardware structure is developed and implemented to further speed up the interpolation process as shown in Fig. 8.

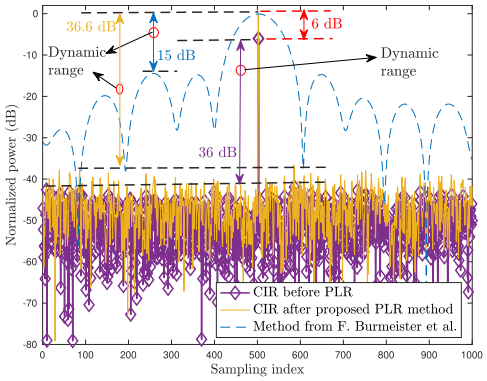

Fig. 9. Comparison of different PLR methods.

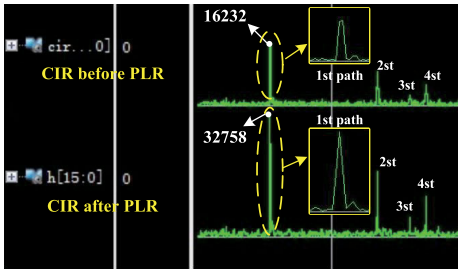

Fig. 10. Hardware output of the PLR module.

The performance of the proposed PLR method is compared with the one of [46] in Fig. 9. To better show the comparison results, we take a one-path CIR obtained from back-to-back measurements as an example. Here, the path power of the selected CIR has a 6-dB loss, and the original dynamic range is about 36 dB. We find that the method in [46] can decrease the power loss to 0.088 dB, but the dynamic range of recovered CIR is only about 15 dB. In our method, the power loss decreases to 0.025 dB, and the dynamic range remains almost unchanged. Moreover, we implement the PLR method in FPGA and give the fixed-point output in Fig. 10, where the parameters are set as follows $N = 1024$, $I = 8$, and $\varepsilon = 1$. A four-path CIR is fed to the PLR module, where each path has a 6-dB power loss. Taking the first path as an example, the fixed-point value of the original path amplitude and recovered path amplitude are 16 232 and 32 758, respectively, which means that the 3-dB amplitude loss, that is, 6-dB power loss is compensated. Note that the power loss of the other three paths is also well compensated.

C. Real-Time MPC Recognition

For the nonstationary A2G channel measurement, it is a great burden on saving extracted CIRs in real-time due to highly dynamic scenarios. For example, if the sampling rate for quadrature CIR is 100 Ms/s, the bit width of CIR is 16 bits, and the storage size of CIRs would be 1.49 GB/s when using four receiving antennas. In this article, we estimate the key channel parameters (or valid MPC information) from the measured CIRs and then only store them in real time. Such a way can greatly remove the storage restriction, but its challenge is obtaining the MPC information under the noise background within each stationary time interval.

The commonly adopted method recognizes the valid MPCs based on a constant noise threshold [53], [54]. In this method,

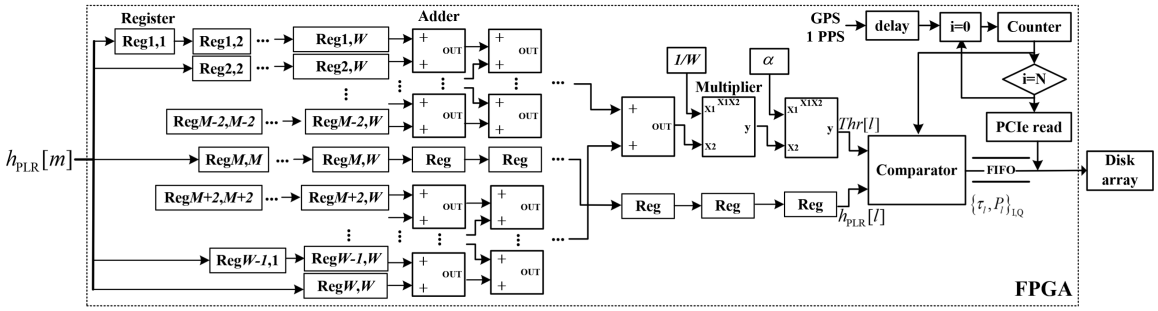

Fig. 11. Real-time structure of adaptive MPC recognition.

the threshold is normally set 20 or 30 dB lower than the power of the strongest path, so it is likely to bring in some fake multipaths under low signal-to-noise ratio (SNR) conditions or eliminate low-power multipaths when the power of the strongest path is much higher than those of the other paths. The constant false alarm rate (CFAR) method with an adaptive noise threshold is a better option [55]. The threshold is adaptively calculated according to the noise level, so only the valid paths whose powers are really close to the noise level would be wrongly eliminated. In general, the utilized solution will greatly decrease the probability of the wrong elimination compared with the constant threshold method. In this method, each sample of the CIR is defined as a cell. The cell under test is defined as a detection cell. The threshold is determined by taking a block of cells around the detection cell and calculating the weighted average power level. Note that couples of cells immediately adjacent to the detection cell, which are referred to as guard cells, are normally excluded to avoid corruption from the power of the detection cell itself. Considering both the denoising performance and hardware complexity, we adopt the dynamic noise threshold with two guard cells as

$$\mathrm{Thr}[l] = \frac{\xi}{W-3}\left(\sum_{w=l-\frac{W-1}{2}}^{l-2} h_{\mathrm{PLR}}[w] + \sum_{w=l+2}^{l+\frac{W-1}{2}} h_{\mathrm{PLR}}[w]\right) \quad (8)$$

where W is the sliding window size for denoising, and $\xi = (W-3)\cdot(p^{-1/(W-3)}-1)$ is the threshold factor, where p is the probability of false alarm. The valid MPC information can be recognized by

$$\mathbf{S}_{\mathrm{I,Q}} = \left\{ \begin{array}{l} \tau_l|_{\mathrm{I,Q}} = i \cdot T_{\mathrm{RX}},\ \alpha_l|_{\mathrm{I,Q}} = h_{\mathrm{PLR}}[l]|_{\mathrm{I,Q}} \\ \text{when peak}(h_{\mathrm{PLR}}[l]) > \mathrm{Thr}[l] \end{array} \right\} \quad (9)$$

where i is the output of counter, $|_{\mathrm{I,Q}}$ means complex number, T_{RX} is the sampling interval of RX, and τ_l and α_l are the path delay and amplitude, respectively. The real-time structure of MPC recognition is shown in Fig. 11. In (8), we can see that $W-3$ reference cells need to be summed up in one sampling clock cycle. Therefore, the registers are utilized to buffer the history cells, and the parallel summation is implemented by using multilayer adders. To compensate for the effect of pipeline latency on the measured path delay, the 1-PPS triggering signal of the GPS module is also delayed according to the value of pipeline latency.

To verify our adaptive MPC recognition module, a time-variant CIR with noise is fed as shown in Fig. 12. The amplitudes of several non-line-of-sight (NLoS) paths are set

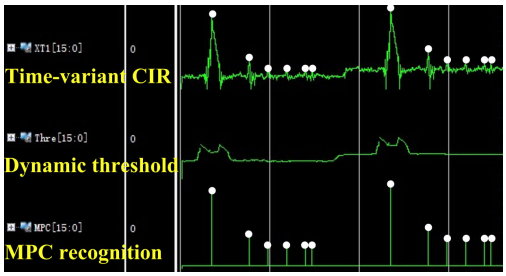

Fig. 12. Hardware output of adaptive MPC recognition.

close to the noise level, and the noise level of the second channel state is higher than that of the first one. Note that it is impossible to recognize all valid paths if we use a fixed threshold. However, the valid multipaths are well extracted by using the proposed adaptive threshold algorithm as shown in Fig. 12.

In the developed channel sounder, only the extracted MPC information needs to be stored in real time. Assuming the average number of valid paths is ten and the length of the ZC sequence is 1024, the storage size of the above example decreases from 1.49 GB to 14.9 MB per second, which would greatly ease the burden of disk space, system data transferring rate, and subsequent data analysis. The comparison of time consumption and data size per second are shown in Fig. 13. In addition, we also develop a software-based method to process the channel data including CIR extraction, PLR, and MPC recognition in real time. The software is developed on a computer with Intel i5-8250U CPU and 16-GB RAM, where Labview 2015 is used as the developing tool. It is found that the time consumption is about 370 ms for one slice of CIR, while the FPGA-based method only consumes 10.24 μs. Moreover, under the working clock frequency of 100 MHz, the consumptions of several hardware resources such as logic slices, flip-flops, LUTs, block RAMs, and DSP slices are 51.7% (32 847/63 550), 19.2% (97 802/508 400), 32.6% (82 823/254 200), 30.1% (239/795), and 13.2% (203/1540), respectively, in the utilized FPGA chip of the Xilinx Kintex-7 410T series.

IV. Measurement Results and Analysis

A. Verification and Calibration

For the A2G channel measurement, the essential parameters are path delay, angle, and amplitude. In this section, a commercial channel emulator (EB Propsim C8) is used to verify and calibrate the measured results of path delay and amplitude. In addition, a signal generator (Agilent E4438C)

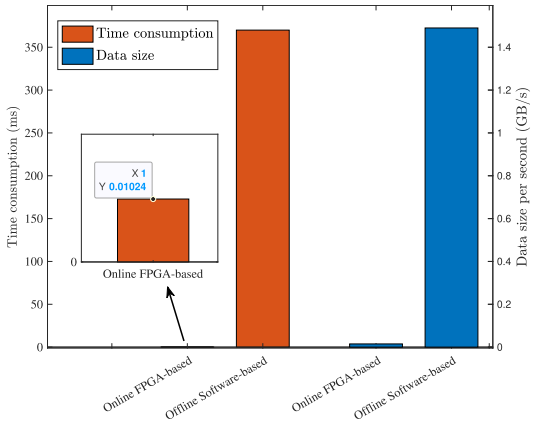

Fig. 13. Comparison of time consumption and data size.

and a power splitter are used to align the phases of different RF channels to ensure accurate angle estimation.

The TX and RX of the channel sounder are connected to the input and output of the channel emulator, respectively, as shown in Fig. 14. For the nonstationary channel, it can be considered as a series of stationary channels along the time sequence. This verification methodology is also employed in the other time-variant channels [56], [57]. Here, we just choose one of those stationary channels to perform the verification. A preset channel with four paths is generated by the channel emulator as shown in Fig. 15(a). The relative path delays are set as 0, 200, 300, and 375 ns, and the relative path amplitudes are 0, −10, −14, and −16 dB, respectively. The measured CIR by the proposed channel sounder is shown in Fig. 15(b). The measured path delays are 0, 200, 300, and 370 ns, and the relative path amplitude is 0, −9.993, −13.517, and −15.813 dB. We can find that there is a 5-ns deviation in the measured path delay of the fourth path due to the 10-ns delay resolution of the developed channel sounder. Moreover, the maximum error of path amplitude is about 1.17%, which is caused by the output resolution of the channel emulator (±0.2 dB) and data processing of the proposed system. Anyway, the measured results are well consistent with the preset ones. In this trial, the SNR of the added white Gaussian noise (AWGN) model in the channel emulator is set to 30 dB. When the SNR decreases, only the noise level of the measured CIR will increase gradually, while the dominant MPC information is approximately unchanged. In Fig. 12, we have verified that the threshold of MPC recognition is adaptive to different noise levels, so the MPCs above the noise level still can be recognized under different SNR conditions. It needs to be clarified that in this article we do not aim to recognize the multipaths hidden in the noise ground.

In this article, the L-shaped antenna array is applied at the ground RX to measure the arrival angle of receiving signal. The angle is estimated based on the phase offsets of the received signal in different RF channels. Therefore, it is important to align the phase between different RF channels before channel measurement. The calibration of phase alignment for the ground RX is shown in Fig. 16(a). The signal generator is connected to the power splitter, where the transmitted single-tone signal is split into four signals.

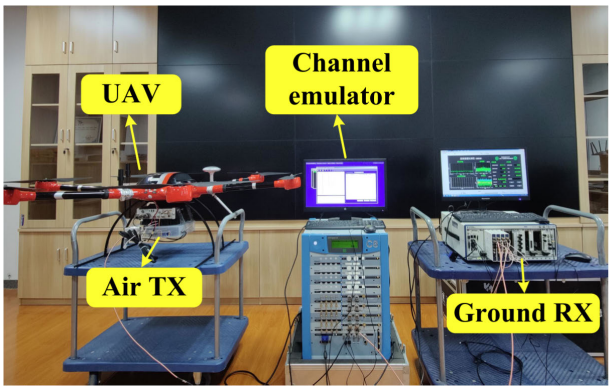

Fig. 14. Overview of A2G channel sounder verification.

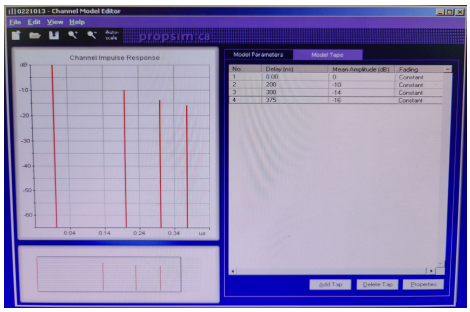

(a)

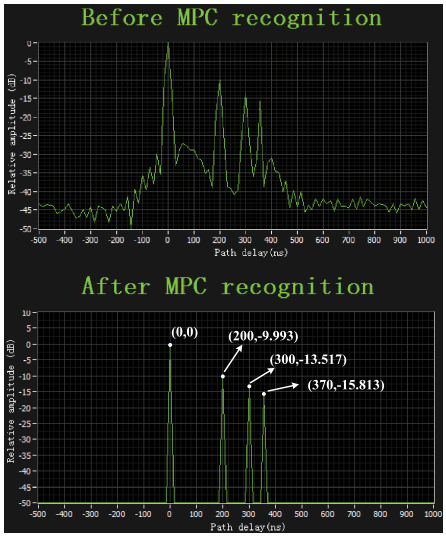

(b)

Fig. 15. (a) Preset CIR of channel emulator and (b) measured CIR of the proposed channel sounder.

The relative phases of different RF channels before and after calibration are shown in Fig. 16(b). It can be found that the final phase deviations of other RF channels to RF channel 1 are below 0.2° which can meet the angle resolution requirement of channel measurement.

B. Application and Analysis

In this section, we carry out the A2G channel measurements by using the developed instrument at 3.5 GHz in a campus scenario. The ground RX is placed on the rooftop with a height of 25 m, which is similar to the communication scenario of UAV to the base station. The UAV experiences several flight phases including takeoff, cruise, and landing as shown

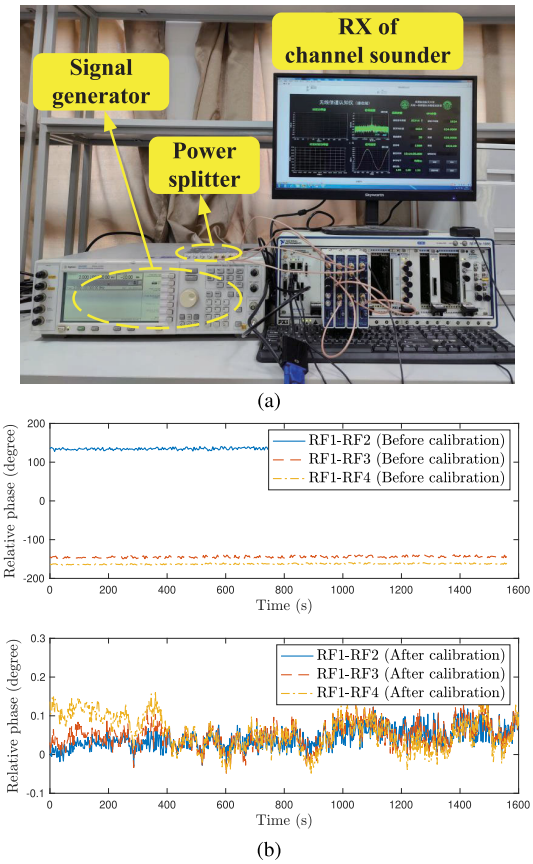

Fig. 16. (a) Overview of phase alignment for the ground RX and (b) phase offsets of RF channels to RF channel 1 before and after calibration.

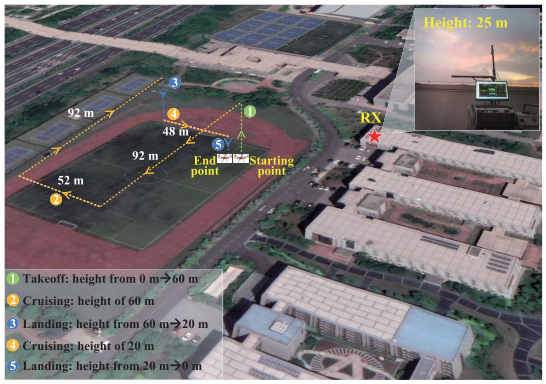

Fig. 17. A2G channel measurement scenario.

in Fig. 17. It takes off from the ground to the height of 60 m and cruises at the height of 60 m. Then, it lands from 60 to 20 m and cruises at 20 m before landing on the ground with a velocity of 2 m/s. In the measurement, the length of the sounding signal is set as 1024 and the CIR is periodically captured. The measurement time interval of each CIR is 10.24 μs, that is, a distance interval of 2.048×10^{-5} m. It is enough to capture the nonstationary channel properties of UAV communication scenarios. Note that the total file size of stored channel data decreases from 300.98 to 1.47 GB by storing valid MPC information of CIR instead of original received signals or CIRs.

The measured CIRs along the whole UAV trajectory are shown in Fig. 18. As shown, the NLoS case (without the

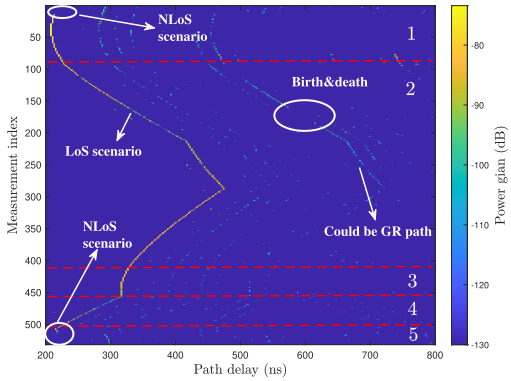

Fig. 18. Measured CIRs of the dynamic nonstationary A2G channel.

LoS path) occurs at the beginning of the first flight phase and the end of the fifth flight phase because the LoS path is more easily blocked by buildings or tall trees when the UAV is at a low height. According to the geometric information of the transceiver, we can obtain that the LoS distance varies from 65 to 145 m, which corresponds to a reference path delay between 216.66 and 483.33 ns. It can be found that the measured path delay values are comparable to the reference ones. For the LoS scenario, if the ground reflection (GR) exists, it can be calculated that the length of the GR path is 132–208 m or the reference path delay is 440–693.33 ns. Therefore, the marked path in Fig. 18 could be the GR path. Due to the motion of UAVs and scatterers, the signal propagates along with the disappearance of existing propagation paths and the appearance of new propagation paths. This process is normally called the birth–death phenomenon, which is an important part of channel modeling [58], [59]. The birth and death phenomena can be clearly observed in the measured results.

The variance of equivalent antenna gain in the elevation plane could be 10 dB as shown in Fig. 3, which must be considered in the path power measurement. The angle of the LoS path can be theoretically calculated by the geometric information of transceivers, so the antenna factor on the power of the LoS path can be calculated and removed. For the NLoS path, we find that the mean elevation angle is about 4° in this measurement scenario, where the antenna gain is close to 0 dBi. Since the deviation of antenna gain between the path angle and the mean angle can compensate for each other when the power of NLoS paths is summed up in the subsequent data processing, the power modification of NLoS paths can be ignored.

The valid MPC information extracted by (9), that is, path delay and complex path amplitude, are stored in the disk. Based on these data, we can further obtain other important channel characteristics, that is, PL, K-factor, and angle distribution.

1) Path Loss: The PL is defined as the ratio of the transmitted power to the received power, which is important for the link budget of UAV communications. It can be obtained from the stored amplitude information as

$$\mathrm{PL}(t) = 10\log_{10}\left(\sum_{l=1}^{L}\alpha_l^2(t)\right) \tag{10}$$

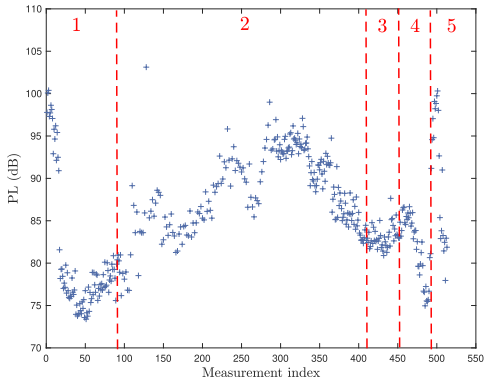

Fig. 19. Measured PLs at different flight phases of UAV.

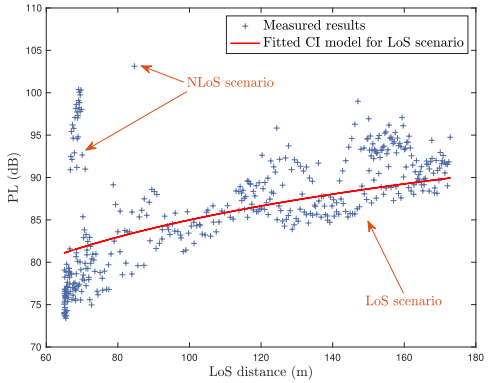

(a)

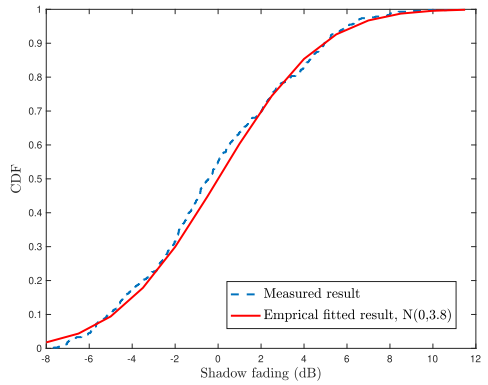

(b)

Fig. 20. (a) Measured and fitted PLs at different LoS distances. (b) Measured and fitted cdfs of shadow fading in CI model.

where α_l is the amplitude of the lth path, and L is the valid path number. The measured PLs along different flight phases of UAV are shown in Fig. 19. Note that the CIRs are sampled with a distance interval of 0.8 m from the whole dataset to ease the burden of data processing. The PLs are time-variant as the communication distance is changing along the UAV flight trajectory. To further obtain the statistical properties of PLs with respect to the communication distances, the commonly used close-in (CI) model is applied to fit the measurement data. It can be expressed as [60], [61]

$$\mathrm{PL}(d(t)) = \mathrm{PL}(d_0) + 10n\log_{10}\left(\frac{d(t)}{d_0}\right) + X_\sigma \qquad (11)$$

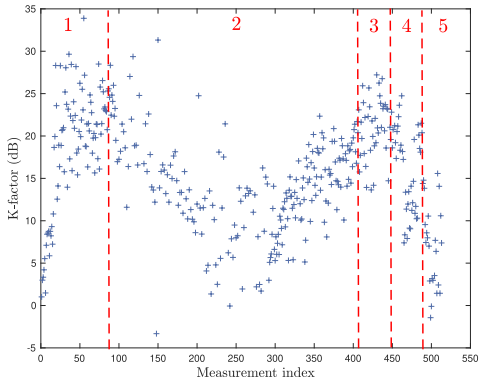

(a)

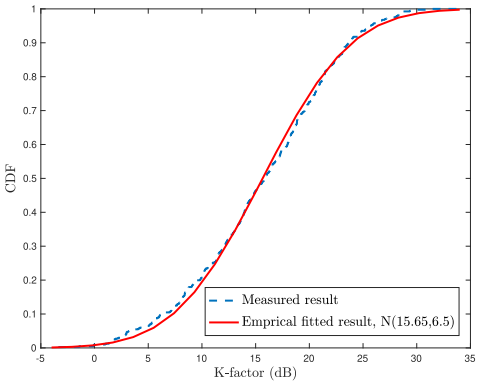

(b)

Fig. 21. (a) Measured K-factors at different flight phases of UAV. (b) Measured and fitted cdfs of K-factor.

where d is the communication distance, namely "LoS distance" for the LoS scenario in this article, $\mathrm{PL}(d_0)$ is the free space PL with $d_0 = 1m$, n is the PL exponent, and X_σ is the shadow fading described by a Gaussian random variable with zero mean and standard deviation σ. The measured and fitted PLs at different LoS distances are given in Fig. 20(a). It can be found that the PLs in the NLoS scenario are about 20 dB higher than that in the LoS scenario. The measured PLs in the LoS scenario are fitted by the CI model where the PL exponent n is 2.077. The shadow fading in the CI model is fitted by the zero-mean Gaussian distribution. The measured and fitted cumulative distribution functions (cdfs) are also compared in Fig. 20(b), where $N(0, 3.8)$ means fit Gaussian distribution with zero-mean and standard deviation σ of 3.8 dB. Note that both the fitted PL exponent n and standard deviation σ are very similar to the measured results under a near-urban scenario in [62].

2) K-Factor: The K-factor is defined as the ratio of path power of the dominant (or LoS) component to the other (or NLoS) components. It is an important parameter to characterize the multipath effect and can be expressed by

$$K(t) = 10\log_{10}\left(\alpha_1^2(t) \Big/ \sum_{l=2}^{L} \alpha_l^2(t)\right). \qquad (12)$$

The measured K-factors along different flight phases of UAV are shown in Fig. 21(a). We find that the tendency of the K-factor pattern in Fig. 21(a) is almost opposite to that of the PL pattern in Fig. 19, which indicates that the K-factor

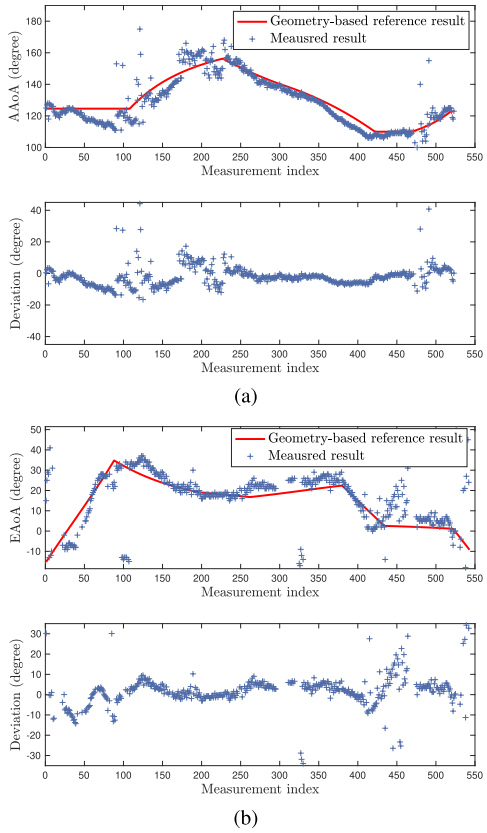

Fig. 22. Measured (a) AAoAs and (b) EAoAs of LoS paths.

is also associated with the communication distance in this measurement scenario. Moreover, the measured and fitted cdf of K-factors are shown in Fig. 21(b). The mean of the K-factor is 15.65 dB, and the standard deviation is 6.5 dB, which means that the LoS scenario is dominant in this measurement scenario and the power of the LoS path is much stronger than that of NLoS paths.

3) Path Angles: The developed channel sounder is capable of estimating the AAoA and EAoA at the ground side. It is valuable to modify angle-related antenna gain and provide a reference for the antenna design of the ground base station such as the antenna tilt angle. Based on the stored CIRs from different antenna elements, we use the space-alternating generalized expectation-maximization (SAGE) algorithm [63] to estimate both AAoAs and EAoAs offline. Note that the angle of the LoS path can also be theoretically estimated by the geometric information, which can be used to validate the angle estimation of the proposed channel sounder. The measured AAoAs and EAoAs of LoS paths along with different flight phases of UAV are shown in Fig. 22. It can be found that both the measured AAoAs and EAoAs of LoS paths are well consistent with the geometry-based theoretical results, which shows the reliability of both the developed channel sounder and the angle estimation algorithm. The geometry-based reference angles are calculated from the transceivers' positions, which could be distorted due to the limitation of the accuracy of GPS positioning. Moreover, although the phase deviations due to RF component imperfection are calibrated in Section IV-A, there are still residues that could slightly affect the estimation accuracy of measured path angles. Therefore, there are some deviations between the reference and the measured results of AAoAs and EAoAs of LoS paths.

V. Conclusion

This article has developed an efficient, accurate, and flexible A2G channel sounder for dynamic communication scenarios. In the channel sounder, a GPS-available triggering signal is designed first for time synchronization to enable absolute path delay measurement. Second, the equivalent antenna pattern on the UAV side has been considered, which shows that the UAV fuselage could cause up to 10-dB variation of path gain. The ZC sounding signal has been selected for its better performance in terms of complexity, spectrum flatness, and dynamic range. Several real-time data-processing methods, that is, real-time CIR extraction, SRE, PLR, and adaptive MPC recognition have been fully implemented on the FPGA chip for the first time. The results and analysis have demonstrated that the cumulative power loss of SCP has been compensated, and the storage data size has been decreased hundreds of times. Compared with software-based real-time data processing, the processing time has been decreased from 370 ms to 10.24 μs by developed FPGA-based methods. Finally, the developed channel sounder has been calibrated and applied to carry out measurement campaigns at 3.5 GHz in a campus scenario, and several channel characteristics have been analyzed. The developed channel sounder can be used to capture the nonstationary channel characteristics for highly dynamic A2G scenarios, which is valuable to the A2G channel modeling as well as the system design and algorithm optimization of A2G communications. Meanwhile, the proposed real-time data-processing methods will be more beneficial for nonstationary channel measurements with a wide bandwidth (i.e., a high sampling rate) and multiple antennas. In the future, we plan to improve the integration level of the SDR module to support the UAV's antenna array. Moreover, we plan to perform multi-input multioutput channel measurement campaigns at different frequencies in different scenarios to obtain more valuable A2G channel characteristics.

Appendix

Let us set the sampling rates of TX and RX as f_{TX} and f_{RX}, respectively, and the STO as $\Delta f = f_{\mathrm{RX}} - f_{\mathrm{TX}}$. According to the definition of the ZC sequence, the relative phase difference of the adjacent sampling point can be calculated as $2n\pi/N_{\mathrm{ZC}}$. Then, the phase difference caused by STO can be expressed as

$$\Delta\phi' = \frac{2n\pi}{N_{\mathrm{ZC}}} \cdot \frac{\Delta f}{f_{\mathrm{RX}}}. \tag{13}$$

Therefore, the total phase difference after sampling the whole ZC sequence can be calculated as

$$\Delta\phi = \sum_{n=1}^{N_{\mathrm{ZC}}} \frac{2n\pi}{N_{\mathrm{ZC}}} \cdot \frac{\Delta f}{f_{\mathrm{RX}}} = \pi(N_{\mathrm{ZC}}+1) \cdot \frac{\Delta f}{f_{\mathrm{RX}}}. \tag{14}$$

Then, the phase difference after time t can be calculated as

$$\Delta\phi_t = \frac{t f_{\mathrm{RX}}}{N_{\mathrm{ZC}}} \cdot \pi(N_{\mathrm{ZC}}+1) \cdot \frac{\Delta f}{f_{\mathrm{RX}}}. \tag{15}$$

Taking the real part as an example, the SCP with STO can be expressed as

$$R_{\mathrm{STO,I}}(t) = \left| \sum_{n=1}^{N_{\mathrm{ZC}}} \frac{\cos\frac{\pi\mu n(n+1)}{N_{\mathrm{ZC}}} \cdot \cos\left[\frac{\pi\mu n(n+1)}{N_{\mathrm{ZC}}} - \frac{t f_{\mathrm{RX}}(N_{\mathrm{ZC}}+1)\Delta f}{N_{\mathrm{ZC}}(f_{\mathrm{TX}}+\Delta f)}\right]}{N_{\mathrm{ZC}}} \right| \approx \left| \sum_{n=1}^{N_{\mathrm{ZC}}} \frac{\cos\frac{\pi\mu n(n+1)}{N_{\mathrm{ZC}}} \cdot \cos\left[\frac{\pi\mu n(n+1)}{N_{\mathrm{ZC}}} - \pi t\Delta f\right]}{N_{\mathrm{ZC}}} \right|. \quad (16)$$

Let us define the ideal SCP as

$$R_{\mathrm{ideal,I}}(t) = \sum_{n=1}^{N_{\mathrm{ZC}}} \left\{ \cos\frac{\pi\mu n(n+1)}{N_{\mathrm{ZC}}} \cdot \cos\frac{\pi\mu n(n+1)}{N_{\mathrm{ZC}}} \right\} \Big/ N_{\mathrm{ZC}} = 1. \quad (17)$$

It can be found that the SCP in (16) reaches the maximum value $R_{\mathrm{STO,I}}(t) = R_{\mathrm{ideal,I}}(t)$ when $t = q/(\Delta f)$, where q is natural number. Similarly, the image part of SCP is as $R_{\mathrm{STO,Q}}(t) = R_{\mathrm{ideal,Q}}(t)$. Therefore, we can get $R_{\mathrm{STO}}(t) = R_{\mathrm{ideal}}(t)$. When $t = p/(2\Delta f)$ (p is odd number)

$$R_{\mathrm{STO,I}}(t) = \left| \sum_{n=1}^{N_{\mathrm{ZC}}} \left\{ \cos\frac{\pi\mu n(n+1)}{N_{\mathrm{ZC}}} \cdot \sin\frac{\pi\mu n(n+1)}{N_{\mathrm{ZC}}} \right\} / N_{\mathrm{ZC}} \right| = \left| \sum_{n=1}^{N_{\mathrm{ZC}}} \frac{1}{2} \sin\frac{2\pi\mu n(n+1)}{N_{\mathrm{ZC}}} / N_{\mathrm{ZC}} \right| \approx \frac{1}{2}. \quad (18)$$

Therefore, we can get

$$R_{\mathrm{STO}}(t) = \sqrt{\frac{1}{4} R_{\mathrm{ideal,I}}{}^2(t) + \frac{1}{4} R_{\mathrm{ideal,Q}}{}^2(t)} = \frac{1}{2} R_{\mathrm{ideal}}(t) \quad (19)$$

which corresponds to the amplitude loss of 3 dB, that is, the power loss of 6 dB.

REFERENCES

[1] M. Silvagni, A. Tonoli, E. Zenerino, and M. Chiaberge, "Multipurpose UAV for search and rescue operations in mountain avalanche events," *Geomatics, Natural Hazards Risk*, vol. 8, no. 1, pp. 18–33, Oct. 2016.

[2] H. Hellaoui, A. Chelli, M. Bagaa, T. Taleb, and M. Pätzold, "Towards efficient control of mobile network-enabled UAVs," in *Proc. IEEE Wireless Commun. Netw. Conf. (WCNC)*, Marrakesh, Morocco, Apr. 2019, pp. 1–6.

[3] Y. Zhai et al., "AntennaNet: Antenna parameters measuring network for mobile communication base station using UAV," *IEEE Trans. Instrum. Meas.*, vol. 70, pp. 1–17, 2021.

[4] X.-H. You et al., "Towards 6G wireless communication networks: Vision, enabling technologies, and new paradigm shifts," *Sci. China Inf. Sci.*, vol. 64, no. 1, pp. 1–74, Jan. 2021.

[5] Z. Ullah, F. Al-Turjman, and L. Mostarda, "Cognition in UAV-aided 5G and beyond communications: A survey," *IEEE Trans. Cognit. Commun. Netw.*, vol. 6, no. 3, pp. 872–891, Sep. 2020.

[6] X. Li, W. Feng, J. Wang, Y. Chen, N. Ge, and C.-X. Wang, "Enabling 5G on the ocean: A hybrid satellite-UAV-terrestrial network solution," *IEEE Wireless Commun.*, vol. 27, no. 6, pp. 116–121, Dec. 2020.

[7] K. Mao et al., "Machine-learning-based 3-D channel modeling for U2V mmWave communications," *IEEE Internet Things J.*, vol. 9, no. 18, pp. 17592–17607, Sep. 2022.

[8] M. M. Azari, F. Rosas, K.-C. Chen, and S. Pollin, "Ultra reliable UAV communication using altitude and cooperation diversity," *IEEE Trans. Commun.*, vol. 66, no. 1, pp. 330–344, Jan. 2018.

[9] B. Hua et al., "Channel modeling for UAV-to-ground communications with posture variation and fuselage scattering effect," *IEEE Trans. Commun.*, vol. 71, no. 5, pp. 3103–3116, May 2023.

[10] A. A. Khuwaja, Y. Chen, N. Zhao, M.-S. Alouini, and P. Dobbins, "A survey of channel modeling for UAV communications," *IEEE Commun. Surveys Tuts.*, vol. 20, no. 4, pp. 2804–2821, 4th Quart., 2018.

[11] C. Yan, L. Fu, J. Zhang, and J. Wang, "A comprehensive survey on UAV communication channel modeling," *IEEE Access*, vol. 7, pp. 107769–107792, 2019.

[12] L. Angrisani, D. Petri, and M. Yeary, "Instrumentation and measurement in communication systems," *IEEE Instrum. Meas. Mag.*, vol. 18, no. 2, pp. 4–10, Apr. 2015.

[13] A. M. Al-samman, M. H. Azmi, and T. A. Rahman, "A survey of millimeter wave (mm-Wave) communications for 5G: Channel measurement below and above 6 GHz," in *Proc. IRICT*, Kuala Lumpur, Malaysia, Jul. 2018, pp. 451–463.

[14] J. Huang, Y. Liu, C.-X. Wang, J. Sun, and H. Xiao, "5G millimeter wave channel sounders, measurements, and models: Recent developments and future challenges," *IEEE Commun. Mag.*, vol. 57, no. 1, pp. 138–145, Jan. 2019.

[15] M. Lei, J. Zhang, T. Lei, and D. Du, "28-GHz indoor channel measurements and analysis of propagation characteristics," in *Proc. IEEE 25th Annu. Int. Symp. Pers., Indoor, Mobile Radio Commun. (PIMRC)*, Washington, DC, USA, Sep. 2014, pp. 208–212.

[16] Y. Rissafi, L. Talbi, and M. Ghaddar, "Experimental characterization of an UWB propagation channel in underground mines," *IEEE Trans. Antennas Propag.*, vol. 60, no. 1, pp. 240–246, Jan. 2012.

[17] Y. Lv, X. Yin, C. Zhang, and H. Wang, "Measurement-based characterization of 39 GHz millimeter-wave dual-polarized channel under foliage loss impact," *IEEE Access*, vol. 7, pp. 151558–151568, 2019.

[18] Y. Lyu, P. Kyösti, and W. Fan, "Sub-THz VNA-based channel sounder structure and channel measurements at 100 and 300 GHz," in *Proc. IEEE 32nd Annu. Int. Symp. Pers., Indoor Mobile Radio Commun. (PIMRC)*, Helsinki, Finland, Sep. 2021, pp. 1–5.

[19] A. W. Mbugua, W. Fan, K. Olesen, X. Cai, and G. F. Pedersen, "Phase-compensated optical fiber-based ultrawideband channel sounder," *IEEE Trans. Microw. Theory Techn.*, vol. 68, no. 2, pp. 636–647, Feb. 2020.

[20] R. Schulpen, D. Konstantinou, S. Rommel, U. Johannsen, I. T. Monroy, and A. B. Smolders, "Extended range ultra-wideband millimeter-wave channel sounder with over-the-air calibration," in *Proc. 13th Eur. Conf. Antennas Propag. (EuCAP)*, Krakow, Poland, Mar. 2019, pp. 1–5.

[21] Y. Xing and T. S. Rappaport, "Propagation measurement system and approach at 140 GHz-moving to 6G and above 100 GHz," in *Proc. IEEE Global Commun. Conf. (GLOBECOM)*, Abu Dhabi, United Arab Emirates, Dec. 2018, pp. 1–6.

[22] F. T. Faul and T. F. Eibert, "Setup and error analysis of a fully coherent UAV-based near-field measurement system," in *Proc. 15th Eur. Conf. Antennas Propag. (EuCAP)*, Dusseldorf, Germany, Mar. 2021, pp. 1–4.

[23] I. Dey, M. M. Butt, and N. Marchetti, "Throughput analysis for virtual MIMO WSNs over measured MIMO channels," *IEEE Trans. Instrum. Meas.*, vol. 68, no. 1, pp. 297–299, Jan. 2019.

[24] J. Zhang, Z. Zheng, Y. Zhang, J. Xi, X. Zhao, and G. Gui, "3D MIMO for 5G NR: Several observations from 32 to massive 256 antennas based on channel measurement," *IEEE Commun. Mag.*, vol. 56, no. 3, pp. 62–70, Mar. 2018.

[25] C. Gentile et al., "Methodology for benchmarking radio-frequency channel sounders through a system model," *IEEE Trans. Wireless Commun.*, vol. 19, no. 10, pp. 6504–6519, Oct. 2020.

[26] J. Huang, C.-X. Wang, Y. Yang, Y. Liu, J. Sun, and W. Zhang, "Channel measurements and modeling for 400–600-MHz bands in urban and suburban scenarios," *IEEE Internet Things J.*, vol. 8, no. 7, pp. 5531–5543, Apr. 2021.

[27] X. Zhao et al., "Playback of 5G and beyond measured MIMO channels by an ANN-based modeling and simulation framework," *IEEE J. Sel. Areas Commun.*, vol. 38, no. 9, pp. 1945–1954, Sep. 2020.

[28] X. Yin, X. Liu, G. Zheng, A. Saleem, and X. Zhai, "28-GHz channel characterization for a short tunnel," *IEEE Microw. Wireless Compon. Lett.*, vol. 28, no. 12, pp. 1146–1148, Dec. 2018.

[29] W. Khawaja, I. Guvenc, D. W. Matolak, U.-C. Fiebig, and N. Schneckenburger, "A survey of air-to-ground propagation channel modeling for unmanned aerial vehicles," *IEEE Commun. Surveys Tuts.*, vol. 21, no. 3, pp. 2361–2391, 3rd Quart., 2019.

[30] X. Cheng, Y. Li, and L. Bai, "UAV communication channel measurement, modeling, and application," *J. Commun. Inf. Netw.*, vol. 4, no. 4, pp. 32–43, Dec. 2019.

[31] M. Rice, A. Davis, and C. Bettweiser, "Wideband channel model for aeronautical telemetry," *IEEE Trans. Aerosp. Electron. Syst.*, vol. 40, no. 1, pp. 57–69, Jan. 2004.

[32] M. Simunek, F. P. Fontan, P. Pechac, and F. J. D. Otero, "Space diversity gain in urban area low elevation links for surveillance applications," *IEEE Trans. Antennas Propag.*, vol. 61, no. 12, pp. 6255–6260, Dec. 2013.

[33] M. Kvicera, F. Pérez Fontán, J. Israel, and P. Pechac, "A new model for scattering from tree canopies based on physical optics and multiple scattering theory," *IEEE Trans. Antennas Propag.*, vol. 65, no. 4, pp. 1925–1933, Apr. 2017.

[34] H. D. Tu and S. Shimamoto, "A proposal of wide-band air-to-ground communication at airports employing 5-GHz band," in *Proc. IEEE Wireless Commun. Netw. Conf.*, Apr. 2009, pp. 1–6.

[35] T. J. Willink, C. C. Squires, G. W. K. Colman, and M. T. Muccio, "Measurement and characterization of low-altitude air-to-ground MIMO channels," *IEEE Trans. Veh. Technol.*, vol. 65, no. 4, pp. 2637–2648, Apr. 2016.

[36] R. Sun and D. W. Matolak, "Air-ground channel characterization for unmanned aircraft systems—Part II: Hilly and mountainous settings," *IEEE Trans. Veh. Technol.*, vol. 66, no. 3, pp. 1913–1925, Mar. 2017.

[37] Z. Cui, K. Guan, C. Oestges, C. Briso-Rodríguez, B. Ai, and Z. Zhong, "Cluster-based characterization and modeling for UAV air-to-ground time-varying channels," *IEEE Trans. Veh. Technol.*, vol. 71, no. 7, pp. 6872–6883, Jul. 2022.

[38] F. Fuschini et al., "An UAV-based experimental setup for propagation characterization in urban environment," *IEEE Trans. Instrum. Meas.*, vol. 70, pp. 1–11, 2021.

[39] W. Khawaja, O. Ozdemir, F. Erden, I. Guvenc, and D. W. Matolak, "Ultra-wideband air-to-ground propagation channel characterization in an open area," *IEEE Trans. Aerosp. Electron. Syst.*, vol. 56, no. 6, pp. 4533–4555, Dec. 2020.

[40] J. Rodríguez-Piñeiro, T. Domínguez-Bolaño, X. Cai, Z. Huang, and X. Yin, "Air-to-ground channel characterization for low-height UAVs in realistic network deployments," *IEEE Trans. Antennas Propag.*, vol. 69, no. 2, pp. 992–1006, Feb. 2021.

[41] B. Ning et al., "A UAV-aided channel sounder for air-to-ground channel measurements," *Phys. Commun.*, vol. 47, Aug. 2021, Art. no. 101366.

[42] R. M. Gutierrez, H. Yu, Y. Rong, and D. W. Bliss, "Time and frequency dispersion characteristics of the UAS wireless channel in residential and mountainous desert terrains," in *Proc. 14th IEEE Annu. Consum. Commun. Netw. Conf. (CCNC)*, Las Vegas, NV, USA, Jan. 2017, pp. 516–521.

[43] R. Geise, A. Weiss, and B. Neubauer, "Modulating features of field measurements with a UAV at millimeter wave frequencies," in *Proc. CAMA*, Västerås, Sweden, Sep. 2018, pp. 1–4.

[44] Z. Qiu, X. Chu, C. Calvo-Ramirez, C. Briso, and X. Yin, "Low altitude UAV air-to-ground channel measurement and modeling in semiurban environments," *Wireless Commun. Mobile Comput.*, vol. 2017, pp. 1–11, Nov. 2017.

[45] Z. Cui et al., "Low-altitude UAV air-ground propagation channel measurement and analysis in a suburban environment at 3.9 GHz," *IET Microw., Antennas Propag.*, vol. 13, no. 9, pp. 1503–1508, Apr. 2019.

[46] F. Burmeister, R. Jacob, A. Traßl, N. Schwarzenberg, and G. Fettweis, "Dealing with fractional sampling time offsets for unsynchronized mobile channel measurements," *IEEE Wireless Commun. Lett.*, vol. 10, no. 12, pp. 2781–2785, Dec. 2021.

[47] A. Taparugssanagorn and J. Ylitalo, "Characteristics of short-term phase noise of MIMO channel sounding and its effect on capacity estimation," *IEEE Trans. Instrum. Meas.*, vol. 58, no. 1, pp. 196–201, Jan. 2009.

[48] D. Caudill, J. Chuang, S. Y. Jun, C. Gentile, and N. Golmie, "Real-time mmWave channel sounding through switched beamforming with 3-D dual-polarized phased-array antennas," *IEEE Trans. Microw. Theory Techn.*, vol. 69, no. 11, pp. 5021–5032, Nov. 2021.

[49] J. Bian, C.-X. Wang, Y. Liu, J. Tian, J. Qiao, and X. Zheng, "3D non-stationary wideband UAV-to-ground MIMO channel models based on aeronautic random mobility model," *IEEE Trans. Veh. Technol.*, vol. 70, no. 11, pp. 11154–11168, Nov. 2021.

[50] H.-J. Zepernick and A. Finger, *Pseudo Random Signal Processing: Theory and Application*. Hoboken, NJ, USA: Wiley, Jul. 2013.

[51] S. Li, X. Dang, C. Hao, M. H. Shah, and J. Li, "Improved channel sounding using ZC sequences in aeronautical telemetry multipath environments," in *Proc. IEEE 21st Int. Conf. Commun. Technol. (ICCT)*, Tianjin, China, Oct. 2021, pp. 1461–1466.

[52] N. Hosseini and D. W. Matolak, "Wide band channel characterization for low altitude unmanned aerial system communication using software defined radios," in *Proc. Integr. Commun., Navigat., Surveill. Conf. (ICNS)*, Herndon, VA, USA, Apr. 2018, pp. 2C2-1–2C2-9.

[53] Y. S. Meng and Y. H. Lee, "Measurements and characterizations of air-to-ground channel over sea surface at C-band with low airborne altitudes," *IEEE Trans. Veh. Technol.*, vol. 60, no. 4, pp. 1943–1948, May 2011.

[54] Z. Cui, C. Briso-Rodríguez, K. Guan, I. Güvenç, and Z. Zhong, "Wide-band air-to-ground channel characterization for multiple propagation environments," *IEEE Antennas Wireless Propag. Lett.*, vol. 19, no. 9, pp. 1634–1638, Sep. 2020.

[55] V. V. Ovchinnikov, N. V. Ryabova, and A. A. Elsukov, "Adaptive HF signal detection algorithm CFAR and its verification by means of SDR based digital ionosonde with USRP platform," in *Proc. Syst. Signal Synchronization, Generating Process. Telecommun. (SYNCHROINFO)*, Minsk, Belarus, Jul. 2018, pp. 1–5.

[56] F. Zhang, L. Hentilä, P. Kyösti, and W. Fan, "Millimeter-wave new radio test zone validation for MIMO over-the-air testing," *IEEE Trans. Antennas Propag.*, vol. 70, no. 2, pp. 1569–1574, Feb. 2022.

[57] *Study on Radiated Metrics and Test Methodology for the Verification of Multi-Antenna Reception Performance of NR User Equipment (UE)*, document 38.827, v16.8.0, 3GPP, Sep. 2022.

[58] E. T. Michailidis, N. Nomikos, P. Trakadas, and A. G. Kanatas, "Three-dimensional modeling of mmWave doubly massive MIMO aerial fading channels," *IEEE Trans. Veh. Technol.*, vol. 69, no. 2, pp. 1190–1202, Feb. 2020.

[59] T. Zwick, C. Fischer, D. Didascalou, and W. Wiesbeck, "A stochastic spatial channel model based on wave-propagation modeling," *IEEE J. Sel. Areas Commun.*, vol. 18, no. 1, pp. 6–15, Jan. 2000.

[60] T. S. Rappaport, *Wireless Communications: Principles and Practice*, 2nd ed. Upper Saddle River, NJ, USA: Prentice-Hall, 2002.

[61] X. Cai et al., "An empirical air-to-ground channel model based on passive measurements in LTE," *IEEE Trans. Veh. Technol.*, vol. 68, no. 2, pp. 1140–1154, Feb. 2019.

[62] D. W. Matolak and R. Sun, "Air-ground channel characterization for unmanned aircraft systems—Part III: The suburban and near-urban environments," *IEEE Trans. Veh. Technol.*, vol. 66, no. 8, pp. 6607–6618, Aug. 2017.

[63] B. H. Fleury, M. Tschudin, R. Heddergott, D. Dahlhaus, and K. I. Pedersen, "Channel parameter estimation in mobile radio environments using the SAGE algorithm," *IEEE J. Sel. Areas Commun.*, vol. 17, no. 3, pp. 434–450, Mar. 1999.

Kai Mao (Member, IEEE) received the B.S. degree in information engineering and the M.S. degree in electronics and communication engineering from the Nanjing University of Aeronautics and Astronautics, Nanjing, China, in 2016 and 2019, respectively, where he is currently pursuing the Ph.D. degree in communication and information systems.

From 2022 to 2023, he was also a Visiting Ph.D. Researcher with the University of Twente, Enschede, The Netherlands. His research interests include channel sounding, modeling, and wireless channel emulation for UAV communication systems.

Qiuming Zhu (Senior Member, IEEE) received the B.S. degree in electronic engineering and the M.S. and Ph.D. degrees in communication and information systems from the Nanjing University of Aeronautics and Astronautics (NUAA), Nanjing, China, in 2002, 2005, and 2012, respectively.

From October 2016 to October 2017, June 2018 to August 2018, and June 2018 to August 2018, he was also an Academic Visitor with Heriot-Watt University, Edinburgh, U.K. Since 2021, he has been a Professor with the Department of Electronic Information Engineering, NUAA. He has authored or coauthored more than 120 articles in refereed journals and conference proceedings and holds more than 40 patents. His research interests include channel sounding, modeling, and emulation for the fifth/sixth-generation (5G/6G) mobile communication, vehicle-to-vehicle communication, and unmanned aerial vehicle communication systems.

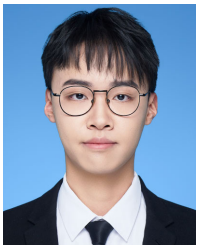

Yanheng Qiu received the B.S. degree in information engineering from the Nanjing University of Aeronautics and Astronautics, Nanjing, China, in 2021, where he is currently pursuing the M.S. degree in information and communications engineering.

His research interests include channel sounding and channel map construction.

Xin Liu (Senior Member, IEEE) received the M.Eng. and Ph.D. degrees in communication engineering from the Harbin Institute of Technology, Harbin, China, in 2008 and 2012, respectively.

From 2012 to 2013, he was a Research Fellow with the School of Electrical and Electronic Engineering, Nanyang Technological University, Singapore. From 2013 to 2016, he was a Lecturer with the College of Astronautics, Nanjing University of Aeronautics and Astronautics, Nanjing, China. He is currently an Associate Professor with the School of Information and Communication Engineering, Dalian University of Technology, Dalian, China. His research interests include communication signal processing, cognitive radio, spectrum resource allocation, and broadband satellite communications.

Maozhong Song received the M.S. degree in communications and electronic systems from Zhejiang University, Hangzhou, China, in 1986.

Since 1986, he has been with the College of Electronic and Information Engineering, Nanjing University of Aeronautics and Astronautics, Nanjing, China, where he is currently a Professor. His research interests include wireless communications and satellite navigation, modulation signal design, signal processing, signal simulator, and embedded systems, and their applications in the Internet of Things.

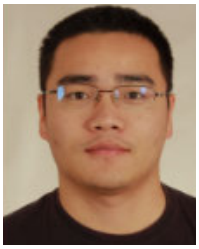

Wei Fan (Senior Member, IEEE) received the B.Eng. degree from the Harbin Institute of Technology, Harbin, China, in 2009, the double master's degree (Hons.) from the Politecnico di Turino, Turin, Italy, and the Grenoble Institute of Technology, Grenoble, France, in 2011, and the Ph.D. degree from Aalborg University, Aalborg, Denmark, in 2014.

From February 2011 to August 2011, he was with Intel Mobile Communications, Aalborg, as a Research Intern. He conducted a three-month internship at Anite Telecoms Oy, Oulu, Finland, in 2014. He is currently an Associate Professor with the Antennas, Propagation and Millimeter-Wave Systems (APMS) Section, Aalborg University. His main research interests include over-the-air testing of multiple antenna systems, radio channel sounding, modeling, and emulation.

André B. J. Kokkeler (Member, IEEE) received the Ph.D. degree in computer science from the University of Twente, Enschede, The Netherlands, in 2005.

He has worked more than six years with Ericsson, Stockholm, Sweden, as a System Engineer and eight years with the Netherlands Foundation for Research in Astronomy (ASTRON), Dwingeloo, The Netherlands, as a Scientific Project Manager. In 2003, he joined the University of Twente, where he is currently a Professor. He has a background in telecommunication, mixed-signal design, and signal-processing architectures. He is involved in research projects, sponsored by the Dutch and European governments and industry. His main research interests include the design of low-power architectures for telecommunications and computationally intensive applications, with a focus on the efficient realization of digital signal processing for communications.

Yang Miao (Member, IEEE) received the M.Sc. and Ph.D. degrees from the Radio Propagation Laboratory, Mobile Communications Research Group, Tokyo Institute of Technology, Tokyo, Japan, in 2012 and 2015, respectively.

From 2010 to 2015, she was a Research Assistant with the Takada Laboratory, Tokyo Institute of Technology. From 2015 to 2018, she was a Post-Doctoral Researcher with the Institute of Information and Communication Technologies, Electronics, and Applied Mathematics, Universite Catholique de Louvain, Louvain-la-Neuve, Belgium, and IMEC, Wireless, Acoustics, Environment, and the Expert Systems Laboratory, Ghent University, Ghent, Belgium. From 2017 to 2018, she was a part-time Senior Antenna Engineer with Jaguar Radio Wave Corporation, Shenzhen, China. From 2018 to 2019, she was a Research Assistant Professor with the Southern University of Science and Technology, Shenzhen. Since August 2019, she has been an Assistant Professor with the Radio Systems Group, University of Twente, Enschede, The Netherlands. Since November 2021, she has also been affiliated part-time with KU Leuven, Leuven, Belgium, as a Marie Curie Individual Fellow. Her research interests include joint communication and sensing, incorporating mobility, and human factors.